PERGAMON

International Journal of Heat and Mass Transfer 45 (2002) 3349–3356

International Journal of HEAT and MASS TRANSFER

www.elsevier.com/locate/ijhmt

An experimental study of heat transfer characteristics of a pair of longitudinal vortices using color capturing technique

E. Kim [a,*], J.S. Yang [b]

[a] School of Mechanical Engineering, Pukyong National University, 599-1 Daeyon 3-Dong, Nam-Ku, Pusan 608-737, Republic of Korea
[b] Research Institute of Mechanical Technology, Pusan National University, 609-735, Republic of Korea

Received 1 March 2001; received in revised form 17 January 2002

Abstract

The flow and heat transfer characteristics of a pair of embedded counter-rotating vortices are studied experimentally. In order to control the strength of longitudinal vortices, angle of attack of the vortex generators is varied from $\pm 20°$ to $\pm 45°$, and the spacing between the vortex generators is 4 cm apart. The heat transfer measurements using thermo-chromatic liquid crystal are made to provide the local surface distributions of heat transfer coefficients. The following conclusions are obtained from the present experiment. For the common-flow-down cases, two maximum values in the local heat transfer distributions exist for the three angles of attack. With the common-flow-up cases, only one maximum value exists. The common-flow-down cases show better heat transfer characteristics than the common-flow-up cases.

1. Introduction

The interaction of vortices and boundary layers occurs in flows of many engineering applications. In turbulent boundary layers longitudinal vortices are generated in many cases naturally or purposely. Recent studies on longitudinal vortices have focused on the interaction of vortices and boundary layers, or on the effect of heat transfer. Also, the proper rules for the design and installation of vortex generators have been studied. Pauley and Eaton [1] studied two types of flow patterns with changing angle of attack of vortex generators; the flow between vortices is away from the wall, common-flow-up, and approaches toward the wall, common-flow-down. Wendt and Hingst [2,3] studied the interaction of vortices and boundary layers occurring downstream of vortex generators, changing the spacing between vortex generators. Eibeck and Eaton [4] have investigated the effects of embedded longitudinal vortices on wall heat transfer. Recently, the studies on the performance of vortex generators, which are used as heat exchangers, have been widely performed. Fiebig [5] noted that longitudinal vortices show less flow loss and better heat transfer characteristics than that of latitudinal vortices. Zhu et al. [6] have also studied the heat transfer effects from longitudinal vortices generated by combining rectangular wings and ribs in a duct. Considering previous studies, the interaction between vortices is an important factor. Other important factors are the spacing between vortices, and the height of vortices from the surface wall. These parameters can be controlled when vortex generators are installed. To control the flow and heat transfer using vortex generators in turbulent boundary layers, a study on the effect of the interaction between vortices is necessary.

In the present study, the experiment is performed with the huge values of angle of attack, β, of vortex generators, $\pm 20°$, $\pm 30°$, $\pm 45°$ compared to previous studies ($-24° \leqslant \beta \leqslant 24°$). The structure of vortices occurring downstream of vortex generators, and the characteristics of heat transfer, are studied using thermo-chromatic liquid crystal [7–12] and a five-hole probe.

2. Experimental apparatus and method

Fig. 1 shows the shape of two half-delta wing vortex generators, and the heat transfer surface instrumented for heat transfer distributions at the downstream of

* Corresponding author. Tel.: +82-51-620-6447; fax: +82-51-620-6446.
E-mail address: ekim@mail.pknu.ac.kr (E. Kim).

0017-9310/02/$ - see front matter
PII: S0017-9310(02)00054-6

Nomenclature

C_p	specific heat at constant pressure of air (kJ/kg K)	T_w	wall temperature of a heating plate (°C)
H	height of a half-delta wing (cm)	U_∞	free velocity of free flow (m/s)
H_{sf}	shape factor	ρ_∞	air density of free flow (kg/m^3)
L	transverse length of a half-delta wing (cm)	δ	thickness of a boundary layer (cm)
Re_L	Reynolds number UL/v	δ^*	displacement thickness (cm)
T_∞	air temperature of free flow (°C)	θ	momentum thickness (cm)

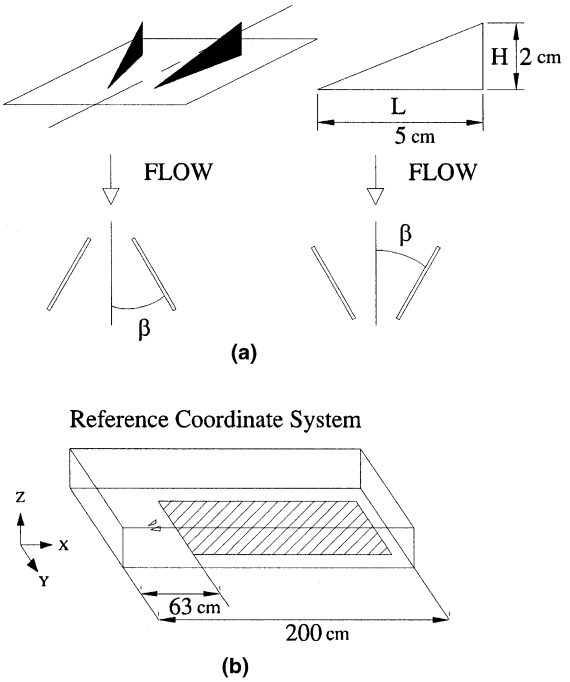

Fig. 1. Schematic diagram of the test facility: (a) half-delta wing; (b) heat transfer surface.

vortex generators. The subsonic wind tunnel which is 10 cm high, 40 cm wide and 200 cm long is used and half-delta wing generators which are 2 cm high and 5 cm long are mounted at 58 cm downstream from the contraction section of the wind tunnel. From the centerline of vortex generators to a clockwise direction, angle of attack, β, is defined as a negative direction. The heat transfer surface is constructed of a stainless steel foil of 40 cm long and 25 cm wide with a thickness of 0.005 cm. The angles of attack of half-delta wing generators in a mainstream direction vary at $\pm 20°$, $\pm 30°$, and $\pm 45°$, and the spacing of half-delta wing generators 4 cm is measured between the generators and the test wall centerline.

A five-hole probe positioned using a three-axis traverse is mounted at 5, 10, 20, and 35 cm downstream of the trailing edge tip of vortex generators. At each location, a slot of 0.4 cm long, 35 cm wide and 0.5 cm thickness in an acrylic plate is made, and a five-hole probe can be moved along the slot to measure the velocity profiles. To prevent the leakage of air in the slot, a sliding plate is attached to a five-hole probe.

A set of pressure data from a five-hole probe is transferred to a pressure transducer (FC044). Then, the pressure data are transformed into digital signals through a multi-channel A/D converter (PCL-718). To reduce errors of pressure data, the pressure values of each pressure hole are collected after 500 measurements, and the total eight dataset with each pressure hole are obtained, and the data of the ensemble mean values of pressure datasets are used [13].

In the heat transfer experiment, a hue-capturing technique using liquid crystal is used, and before measuring the heat transfer field the calibration experiment is conducted for the temperature measurement. A video camera is used for the capture of hue changes with temperature variations of liquid crystal (see Fig. 2). The experiment is conducted in a dark room to block any light except that, which is necessary for the experiment, and the calibration experiment is installed at the same position with the actual experimental section. The distance between the calibration apparatus and the video camera is 150 cm apart, and the angle between the light and the calibration plate is fixed at 60°. To measure the temperature and the hue change of liquid crystal simultaneously with a time constant of 100 Hz, a video camera and a standard temperature system that has an accuracy of ± 0.1 °C are used. The calibration experiment is conducted four times measuring at different times, and Fig. 3 shows the hue versus temperature profiles of liquid crystal. From these results, ensemble average values are calculated and the calibration curve to show the variations of hue versus temperature is given. The calibration curve equation is the following:

$$T = 34.967 + 0.048852 \times \mathrm{Hue} - 0.0017587 \times \mathrm{Hue}^2 + 1.793 \times 10^{-5} \times \mathrm{Hue}^3 - 6.303 \times 10^{-8} \times \mathrm{Hue}^4. \quad (1)$$

Fig. 4 shows the experimental apparatus to measure the heat transfer characteristics developed by vortex

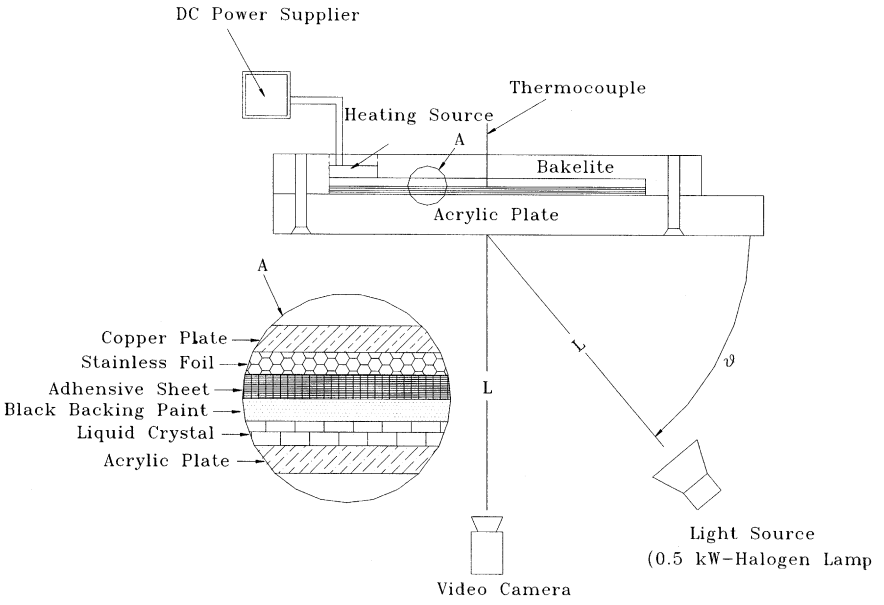

Fig. 2. Schematic diagram of calibration apparatus for local hue versus temperature relation.

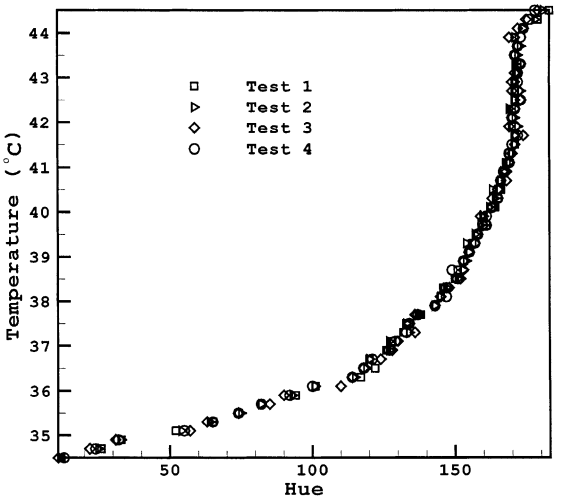

Fig. 3. Local hue versus temperature relation.

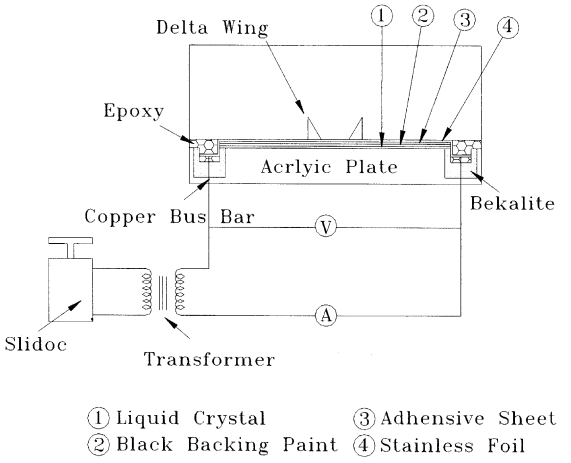

Fig. 4. Experimental apparatus for the measurement of heat transfer rate on the wall surface.

generators with varying angles of attack. On an acrylic plate (1 cm thick, 40 cm wide, and 40 cm long), the liquid crystal (R35C5W) is airbrushed. To absorb unnecessary light, black backing paint is uniformly sprayed on a liquid crystal film, and to heat liquid crystal a stainless steel foil (0.005 cm × 40 cm × 25 cm) is used. Also, a copper bar with 0.1 cm diameter is attached at both sides of the stainless steel foil. A uniform heat flux is produced by passing a current across the stainless steel foil via copper bars at both sides [8]. A Bakelite plate is used to block the heat from the copper pipe. The resistive heating can be determined by measuring the current passing through the stainless steel foil and the voltage drop across the length of the heated surface.

3. Experimental results and discussion

To investigate the flow characteristics in the test section, mean velocity, boundary layer thickness, and turbulence intensity are measured using I type hotwire probes and boundary layer probes. A starting position is

located 58 cm downstream from the contraction section of the wind tunnel, and parameters are measured with 0.05 cm intervals from the bottom wall using a three-axis traverse. Experimental conditions calculated for the present experiment are shown in Table 1. The flow characteristics with common-flow-down and common-flow-up are described in Han's paper [14] in detail. In this paper, the results are presented only for $\pm 30°$ angles of attack. Since a five-hole probe measures a higher pressure on the upper pressure tap than on the lower pressure tap in the boundary layer, pressure data of a five-hole probe measured in the boundary layer contain significant errors. Therefore, the secondary flows measured with a five-hole probe are corrected by the correction method of Westphal et al. [15]. Fig. 5 shows the velocity vectors of secondary flows with common-flow-down for 30° angle of attack at several positions. Vortex pairs are counter-rotating; one circulates in a counter clockwise direction and the other in a clockwise direction. It is clear that as the flow moves to a downstream direction, the velocity vectors of vortex pairs decrease by the conservation of angular momentum and turbulent diffusion, and the distances between vortex pairs increase. Fig. 6 shows the secondary velocity vectors of the common-flow-up case at $X = 5$, 10, 20, 35 cm with $-30°$ angle of attack. A vortex pair occurs; one vortex rotates to a clockwise direction, and the other to a counter clockwise direction. A counter-rotating vortex makes an up-wash flow around the centerline, and a downwash flow at the outer section of the central region. It is seen

Table 1
Experimental conditions

Boundary layer thickness (δ)	1.3 (cm)
Displacement thickness (δ^*)	0.417 (cm)
Momentum thickness (θ)	0.275 (cm)
Shape factor ($H_{sf} = \delta^*/\theta$)	1.52
Reynolds number ($Re_L = U_\infty L/\nu$)	31 400
Turbulent intensity	0.6 (%)

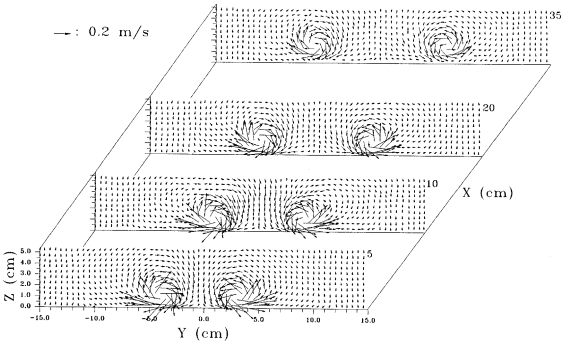

Fig. 5. Secondary velocity vectors at $\beta = 30°$.

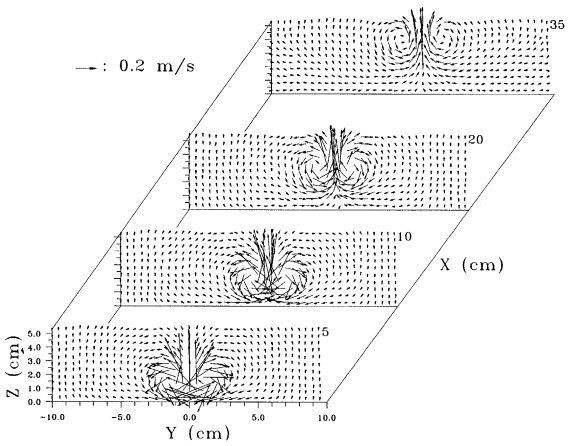

Fig. 6. Secondary velocity vectors at $\beta = -30°$.

clearly that the common-flow-up vortices interact strongly with each other. Therefore, as the measured positions move to the downstream of vortex generators, the velocity vectors decrease and the distance between vortices barely change which is as much as in the common-flow-down case. However, the rising trend of the vortices from the wall increases. These phenomena are also observed in the experiment of Pauley and Eaton [1].

The local heat transfer characteristics occurring downstream of half-delta wings can be represented by the Stanton number as follows:

$$St = \frac{\dot{q}}{\rho_\infty C_p U_\infty (T_w - T_\infty)}. \tag{2}$$

The uncertainty analysis of the Stanton number has been carried out using the methods of Holman [16] and Abernethy et al. [17]. It is shown in Table 2 that the total uncertainty in the Stanton number is 5.4%. In calculating the uncertainty, the specific heat, C_p, is assumed to be a constant because it is not sensitive on the range of the parameters of the present experiment.

The heat transfer coefficients for the contour developments of vortices represented by the Stanton number with the common-flow-down cases at 20°, 30°, and 45° angles of attack are shown in Fig. 7. In the figure, the Stanton number has a unit of $St \times 1000$, and the contour lines show at each 0.00015 interval. At 45° angle of attack, two maximum heat transfer values over the whole domain exist (see Fig. 7(c)). At 30° angle of attack, there are also two maximum heat transfer values after $X =$ 10 cm. At 20° angle of attack, it occurs after $X = 15$ cm. As the angle of attack increases, the distance between vortices increases. This causes the interaction between vortices to weaken. Thus, the local heat transfer distributions having two maximum values are shown over the whole domain. The positions of each maximum value almost agree with the centerline positions of vortices,

Table 2
The uncertainty of the Stanton number with odds of 20 to 1

X_i	Value	δX_i	$(\delta X_i/X_i) \times 100$ (%)
V	2 (V)	0.12 (V)	0.6
I	46 (A)	1 (A)	2.17
A	0.105 (m^2)	0.001 (m^2)	0.95
ρ_∞	1.2822 (kg/m^3)	0.0111 (kg/m^3)	0.87
U_∞	10 (m/s)	0.23 (m/s)	2.3
δ (ΔT)	8.0 (°C)	0.33 (°C)	4.125
Total Stanton number uncertainty $\delta(St)/St = 5.38$ (%)			

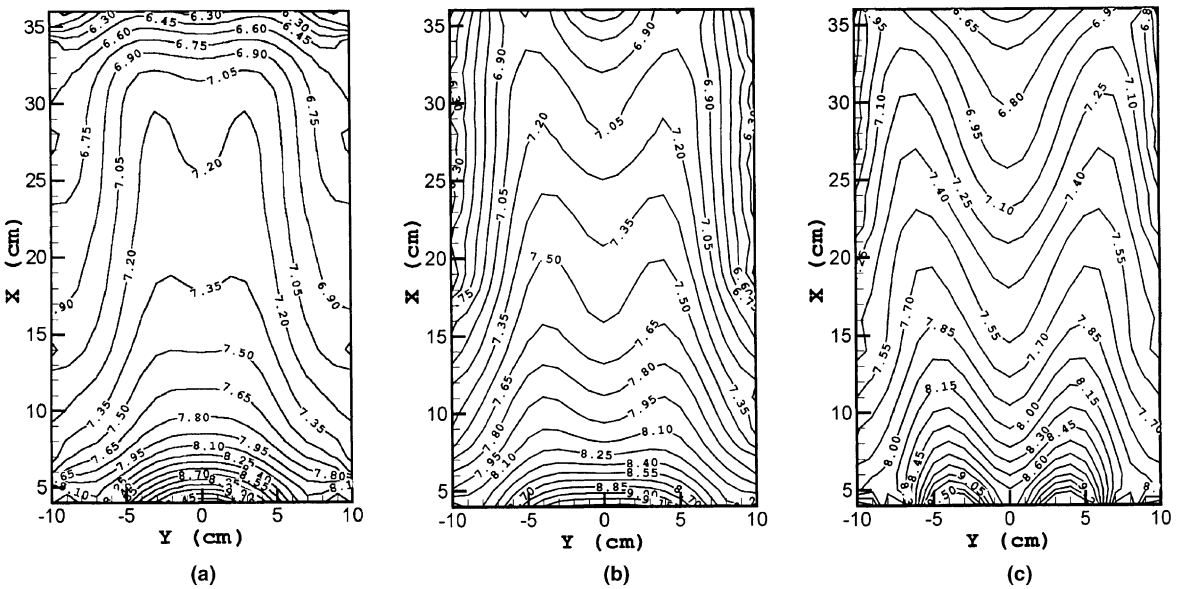

Fig. 7. Temperature contours for (a) $\beta = 20°$, (b) $\beta = 30°$, and (c) $\beta = 45°$ angles of attack.

and occur when the vortices developed from vortex generators are attached at the surface of the wall to the downwash domain. Fig. 8 shows the heat transfer coefficients of the whole wall with the common-flow-up cases at $-20°$, $-30°$, and $-45°$ angles of attack. At $-20°$ angle of attack, the two maximum values are shown up to $X = 30$ cm: at $-30°$ angle of attack, it is shown to $X = 20$ cm: and at $-45°$ angle of attack, the local heat transfer distributions have only one maximum value over the entire domain. This means the interaction between vortices is strong when the angle of attack decreases. The positions of two maximum heat transfer values are almost the same with the vortex centers. After $X = 30$ cm, only one maximum heat transfer value exists for all three angles of attack. By the interaction between vortices, the positions of vortices rise from the wall (see Fig. 6). The distance between two maximum heat transfer values does not change clearly when the angle of attack is decreased.

Figs. 9–12 show the local heat transfer distributions at $X = 5$, 10, 20, and 35 cm for the common-flow-downs. For 45° angle of attack, two maximum values exist. However, for 20° and 30° angles of attack one maximum value exists. For all cases of angle of attack, at least two minimum heat transfer values exist. In general, these two minimum values occur when flow produced by vortex generators moves from a downwash domain to an up-wash domain. The heat transfer gradient along a spanwise direction is the largest for 45° angle of attack. For 45° angle of attack, the maximum heat transfer values increase 7% and 3% more than those of 20° and 30° angles of attack, respectively. In Fig. 10, for 20° and 30° angles of attack two maximum values exist at $X = 10$ cm. In Fig. 9 one maximum value for the case of 20° angle of attack exists. Compared with Fig. 9, the positions of maximum and minimum values of the Stanton number move to a spanwise direction. This means that the interaction between vortices in

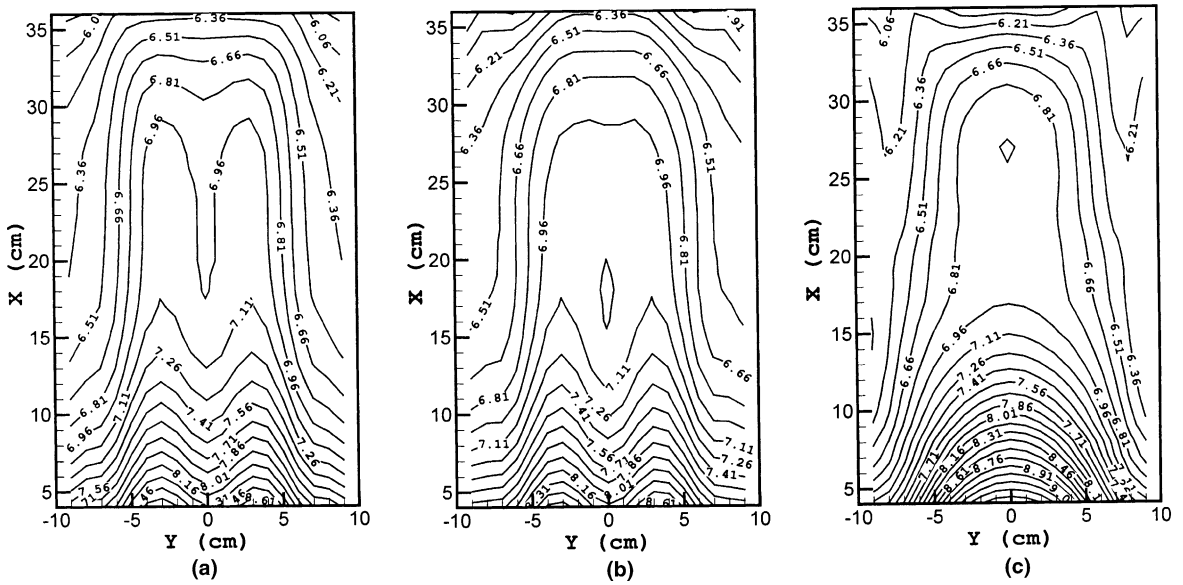

Fig. 8. Temperature contours for (a) $\beta = -20°$, (b) $\beta = -30°$, and (c) $\beta = -45°$ angles of attack.

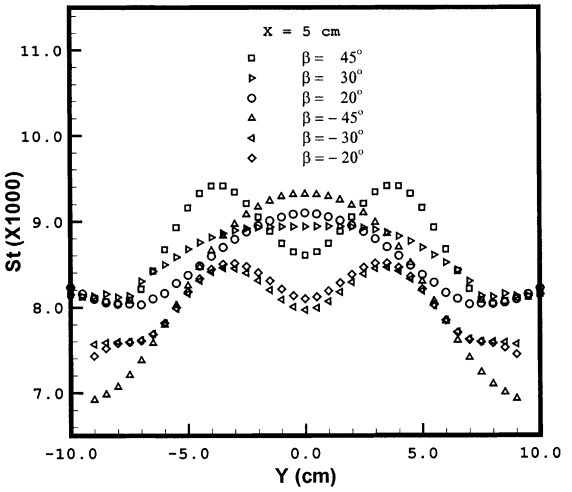

Fig. 9. Spanwise profiles of the Stanton number with $\beta = \pm 20°$, $\pm 30°$ and $\pm 45°$ at $X = 20$ cm.

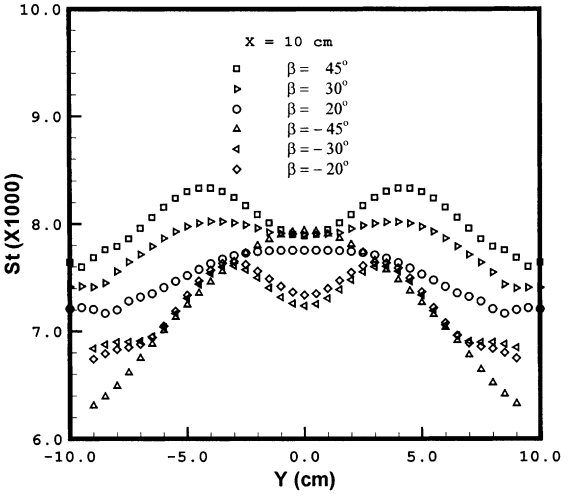

Fig. 10. Spanwise profiles of the Stanton number with $\beta = \pm 20°$, $\pm 30°$ and $\pm 45°$ at $X = 35$ cm.

common-flow-down case becomes weaker. For 45° angle of attack, the maximum Stanton number increases about 9.5% more than for 20° angle of attack and about 4% for 30° angle of attack. Fig. 11 shows the local heat transfer distributions with varying angles of attack at $X = 20$ cm. The two maximum heat transfer values with the common-flow-down cases exist along a spanwise direction. The spacing between maximum values increases as the angles of attack increase. For example, the maximum values increase less for 30° angle of attack than for 45° angle of attack. The overall heat transfer values decrease compared with those of vortices at the upstream location, because turbulence diffusion makes vortices weak. In Fig. 12, the profiles of the heat transfer distributions are similar to Fig. 11. However, for 20° angle of attack, the heat transfer distributions clearly show two maximum heat transfer values. For 30° and 45° angles of attack, the maximum values of heat transfer distributions are almost the same.

Next, the common-flow-up cases in Figs. 9–12 are explained. It is observed from Fig. 9 that for $-20°$ and $-30°$ angles of attack the local heat transfer distribu-

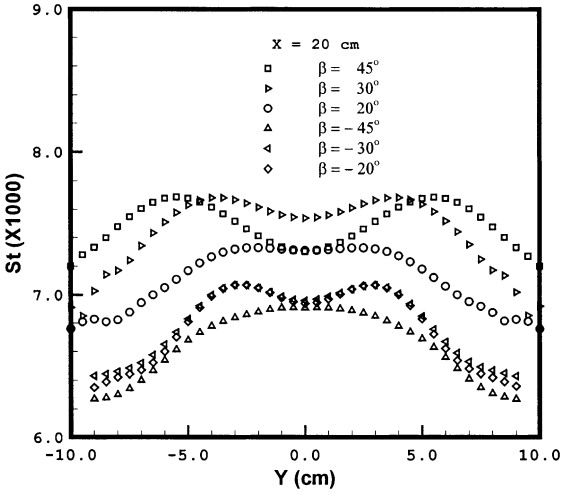

Fig. 11. Spanwise profiles of the Stanton number with $\beta = \pm 20°$, $\pm 30°$ and $\pm 45°$ at $X = 20$ cm.

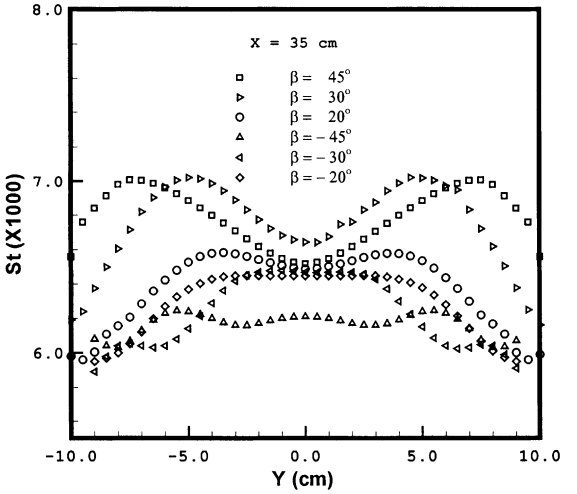

Fig. 12. Spanwise profiles of the Stanton number with $\beta = \pm 20°$, $\pm 30°$ and $\pm 45°$ at $X = 35$ cm.

tions show similar profiles, but for $-45°$ angle of attack one maximum heat transfer value exists. This is because as the angle of attack increases, the interaction between vortices becomes stronger. For $-45°$ angle of attack, the maximum heat transfer value increases about 10.5% more than that of $-20°$ and $-30°$ angles of attack, but for $-20°$ and $-30°$ angles of attack the maximum value does not change clearly. In Fig. 10, the heat transfer distributions for three cases of $-20°$, $-30°$ and $-45°$ angles of attack show a similar profile, but for the case of $-45°$ angle of attack the local maximum heat transfer value increases about 4% more than that of $-20°$ and $-30°$ angles of attack. In Fig. 11, for all three cases the heat transfer distributions show similar profiles compared with the profiles in Fig. 10. However, the maximum heat transfer value for $-45°$ angle of attack is smaller than that for $-20°$ and $-30°$. This is because as the angle of attack decreases, the interaction between vortices becomes stronger, and the rising effect of vortices from the wall increases. In Fig. 12, only one maximum heat transfer value exists for $-20°$ and $-30°$, respectively. After $X = 35$ cm, the rising effect of vortices from the wall becomes stronger.

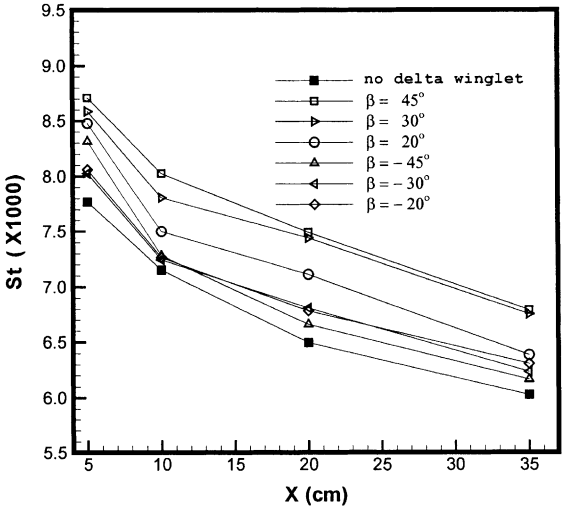

Fig. 13. Streamwise distributions of averaged Stanton number.

Fig. 13 shows the average heat transfer distributions, which are calculated using Simpson' integral method, at selected positions. The average heat transfer for all angles of attack shows similar profiles. After $X = 20$ cm, the decreasing rate of the average heat transfer becomes a constant. For 45° angle of attack, the heat transfer shows the highest value for all positions along a X-direction. Before $X = 10$ cm for all angles of attack, the average heat transfer changes rapidly, and after $X = 10$ cm the heat transfer changes smoothly. For $-20°$ and $-30°$ angels of attack, the average heat transfer shows similar profiles, but the heat transfer values for those two cases increase more than those for $-45°$ angle of attack. Before $X = 10$ cm, the local heat transfer with varying angles of attack changes rapidly, and after that position the trend is smooth. The cases that installed half-delta wings show better heat transfer characteristics than the case with a half-delta wing. The heat transfer shows the best characteristics in the common-flow-down cases.

4. Conclusion

An experimental study has been carried out to investigate the effects of longitudinal vortices embedded in turbulent boundary layers with the common-flow-down

and common-flow-up cases. For the common-flow-down cases, two maximum values in the local heat transfer distributions exist for the three angles of attack. With the common-flow-up cases, only one maximum value exists. As vortex pairs with common-flow-down move to a downstream direction, the interaction of a boundary layer becomes stronger than the interaction between vortices. However, with common-flow-up, the vortex interaction is stronger than that of the boundary layer. The common-flow-down cases show better heat transfer characteristics than the common-flow-up cases.

References

[1] W.R. Pauley, J.K. Eaton, Experimental study of the development of longitudinal vortex pairs embedded in a turbulent boundary layer, AIAA J. 26 (7) (1988) 816–823.
[2] B.J. Wendt, W.R. Hingst, Flow structure in the wake of a wishbone vortex generator, AIAA J. 32 (11) (1994) 2234–2240.
[3] B.J. Wendt, I. Grebert, W.R. Hingst, Structure and development of streamwise vortex arrays embedded in a turbulent boundary layer, AIAA J. 31 (2) (1993) 319–325.
[4] P.A. Eibeck, J.K. Eaton, Heat transfer effects of a longitudinal vortex embedded in a turbulent boundary layer, ASME J. Heat Transfer 109 (1987) 16–24.
[5] M. Fiebig, Vortices and heat transfer, Z. Angew. Math. Mech. 77 (1) (1997) 3–18.
[6] J.X. Zhu, M. Fiebig, N.K. Mitra, Numerical investigation of turbulent flows and heat transfer in a rib-roughened channel with longitudinal vortex generators, Int. J. Heat Mass Transfer 38 (3) (1995) 495–501.
[7] C. Camci, K. Kim, S.A. Hippensteele, P.E. Pointsatti, Evaluation of a hue capturing based transient liquid crystal method for high-resolution mapping of convective heat transfer on curved surfaces, ASME J. Heat Transfer 115 (1993) 311–318.
[8] N. Akino, T. Kunugi, K. Ichimiya, K. Mitsushiro, M. Usda, Improved liquid-crystal thermometry excluding human color sensation, ASME J. Heat Transfer 111 (1989) 558–565.
[9] S.A. Hippensteele, L.M. Russell, F.J. Torres, Local heat transfer measurements on a large scale-model turbine blade airfoil using a composite of a heat element and liquid crystals, ASME J. Eng. Gas Turbines Power 107 (1985) 953–960.
[10] J.S. Yang, J.M. Na, K.B. Lee, An experimental investigation of the heat transfer characteristics on the endwall surface within the plane turbine cascade, KSME J. 19 (1995) 2386–2398.
[11] G.H. Jung, Y.Y. Kim, S.K. Kim, T.B. Seo, An experimental study on the heat transfer augmentation by using the multiple orifice nozzle, SAREK J. 11 (1999) 647–657.
[12] K.B. Lee, T.Y. Kim, J.S. Yang, The natural convection in a three dimensional enclosure using color capturing technique and computation, KSME J. B 21 (1997) 1595–1607.
[13] K.B. Lee, J.S. Yang, The calibration and application of 5-hole probe using cubic spline interpolation, KSAS J. 23 (1995) 61–68.
[14] D.J. Han, An experimental study on the interaction and flow characteristics of longitudinal vortex pairs, MS thesis, Pusan National University, 1999.
[15] R.V. Westphal, J.K. Eaton, W.R. Pauley, Interaction between a vortex and a turbulent boundary in a streamwise pressure gradient, in: Proceedings of Fifth Symposium on Turbulent Shear Flows, Ithaca, NY.
[16] J.P. Holman, Experimental Methods for Engineers, McGraw-Hill, New York, 1984.
[17] R.B. Abernethy, R.P. Benedict, R.B. Dowdell, ASME measurement uncertainty, ASME J. Fluids Eng. 107 (1985) 161–164.